The Version of Record is available at DOI: 10.1016/j.apacoust.2023.109274.

Simulation of acoustic oscillatory flows around a curvature controlled by a plasma actuator

Hiroshi Yokoyama (横山博史)[a,*], Katsuaki Yoza (與座克明)[a],
Masahito Nishikawara (西川原理仁)[a], Hideki Yanada (柳田秀記)[a]

[a] *Department of Mechanical Engineering, Toyohashi University of Technology,*
1-1 Hibarigaoka, Tempaku-cho, Toyohashi, Aichi 441-8580, Japan

In this study, simulations based on the three-dimensional compressible Navier–Stokes equations were conducted to clarify a control method with a plasma actuator to reduce the acoustic power loss in the oscillatory flow under acoustic excitation (acoustic oscillatory flow) in a curved duct. The acoustic power loss for the curved duct exceeds that for the straight duct, particularly at a high acoustic Reynolds number based on the amplitude of the velocity fluctuations in the duct. Flow control by a plasma actuator, which was installed near the curvature in the straight section, was applied to suppress the periodically occurring flow separation around the curvature, which leads to energy loss in the baseline flow. The plasma actuator was intermittently driven at the same frequency as the acoustic oscillatory flow. It was thus demonstrated in the present numerical simulations that the acoustic power loss around the curvature was reduced by the flow control with the plasma actuator. Furthermore, efficient control conditions for the number of plasma actuators and the driving voltage are discussed considering the power consumption of the plasma actuator, although the power efficiency of the control needs to be improved for actual application. Moreover, the relatively effective intermittent control conditions of the phase and duty ratio for the reduction of acoustic power loss are presented with the predicted flow fields around the curvature.

[*] Corresponding author: h-yokoyama@me.tut.ac.jp

Keywords: Minor loss, Curved resonator, Direct aeroacoustic simulation, Plasma actuator, Flow control, Thermoacoustic device

1. Introduction

Thermoacoustic devices [1] that use the interaction between acoustic and thermal energies in narrow channels have been investigated as methodologies for the utilization of waste heat and radiated sound energy. To improve their performance, it is necessary to evaluate and suppress the energy losses generated in ducts with area changes, curvatures, and branches, which are called minor losses [2]. Although the usage of a curved resonator is needed for a small-footprint thermoacoustic device, lowering of the output power for a thermoacoustic engine due to the minor loss of a curvature was reported [3].

Quantitative evaluations of the minor losses have been performed for oscillatory flows under acoustic excitation (acoustic oscillatory flows) in the resonator duct with cross-sectional area change [4,5] and curvature [6]. Wee [7] observed the occurrence of flow separation and vortices leading to energy loss in acoustic oscillatory flows through the curvature by particle image velocimetry. Two-dimensional numerical simulations were performed to investigate the effects of the contraction of a duct on the acoustic oscillatory flow [8,9] using non-dimensional parameters, such as the acoustic Reynolds number and Womersley number. However, the relationship between acoustic power loss and the flow field around the curvature has not been sufficiently clarified. In addition, the suppression of the minor loss by using active flow control has not been investigated, possibly because of the absence of an appropriate flow control device and shortage of knowledge for effective active flow controls.

In this study, to control the acoustic oscillatory flow around a curvature for the suppression of the minor loss, a dielectric barrier discharge plasma actuator (PA) [10] was adopted. The plasma actuator comprises two electrodes separated by a dielectric layer. By applying a high-amplitude and high-frequency AC voltage between two electrodes, the generation of plasma induces a flow from the exposed electrode toward the embedded electrode [11,12]. The plasma actuators have the advantages of a thin structure, easy installation, and fast time response.

Therefore, the plasma actuator is expected to be an effective flow control device, and many studies have been performed mainly for the suppression of flow separation and aerodynamic noise around bluff bodies, airfoils, and cavities in a unidirectional freestream [10,13,14]. The plasma actuator with fast time response is expected to be effective for the control of the acoustic oscillatory flow to suppress the minor loss. However, the control effects of the plasma actuator on acoustic oscillatory flows have not been investigated.

The objective of this study is to evaluate the control effects of the plasma actuator for the suppression of acoustic power loss in a curved resonator and to clarify the suppression mechanism. To this end, control effects on flow and sound fields of the acoustic oscillatory flow were simultaneously predicted by three-dimensional compressible flow simulations. To clarify the relatively effective control methodology, the control effects of the intermittently driven plasma actuator with varied arrangements of the plasma actuator(s) and control conditions are discussed in this paper. This study is novel in that it constitutes the first attempt at presenting the quantitative evaluation of active intermittent flow control in suppressing minor losses in acoustic oscillatory flows with a plasma actuator. Furthermore, this work also introduces a three-dimensional flow field related to the flow separation around the curvature in acoustic oscillatory flows.

2. Methodology

2.1. Flow configurations

Figure 1 shows the configurations of the straight and curved ducts with acoustic excitation. Acoustic excitation was performed on one end of the duct (open end) and the other end was closed. The origin of the coordinate system is located at the center of the cross-section of the open end. The x-axis is along the centerline of the duct from the open end toward the closed end. The y-axis is oriented toward the inner side of the curvature for the curved duct, and the z-axis perpendicular to the x- and y-axes is along the spanwise direction. For both the straight and curved ducts, the centerline length was L = 961 mm, and the cross-section was a square with a side of D = 40 mm. The ducts were then filled with standard air. These resonator conditions were determined by referring to the experimental setup described in a previous study, where the acoustic excitation was performed by a speaker at the open end for the thermoacoustic heat pump (refrigerator) [1,15,16]. Although periodic vortices can be formed around the open end when sound and flow pass through the open end [17], these effects are not considered in this paper.

The excitation frequencies f_a were 268 Hz and 280 Hz for the straight and curved ducts, respectively. The excitation frequencies were determined such that acoustic resonance with a three-quarter wavelength mode occurred. For the curved duct, the curvature with a centerline radius of R_c = 25 mm was located at x_c/L = 0.67, which was corresponding to the position of the antinode of the velocity fluctuations in this acoustic mode and the acoustic power loss due to the curvature were assumed to be large [18]. The pressure amplitude at the closed end for the excitation frequency, $p_{a,c}$, was varied from 1.6 kPa to 7.8 kPa, which corresponded to the acoustic Reynolds number of $\mathrm{Re}_a \equiv u_a D/\nu = 1.0\times10^4$–$5.0\times10^4$ (u_a: amplitude of cross-sectional-averaged velocity fluctuations at the antinode, ν: kinematic viscosity). This range was below the critical Reynolds number for turbulent transition of $\mathrm{Re}_c = 8.5\times10^4$ considering the present Womersley number of $\mathrm{Wo} \equiv (D/2)(2\pi f_a/\nu)^{1/2} = 2.1\times10^2$ [19]. Therefore, the oscillatory boundary layer near the wall was assumed laminar. Note that three-dimensional computations are necessary to capture three-dimensional vortices appearing around the curvature, as discussed in Section 3.2.2.

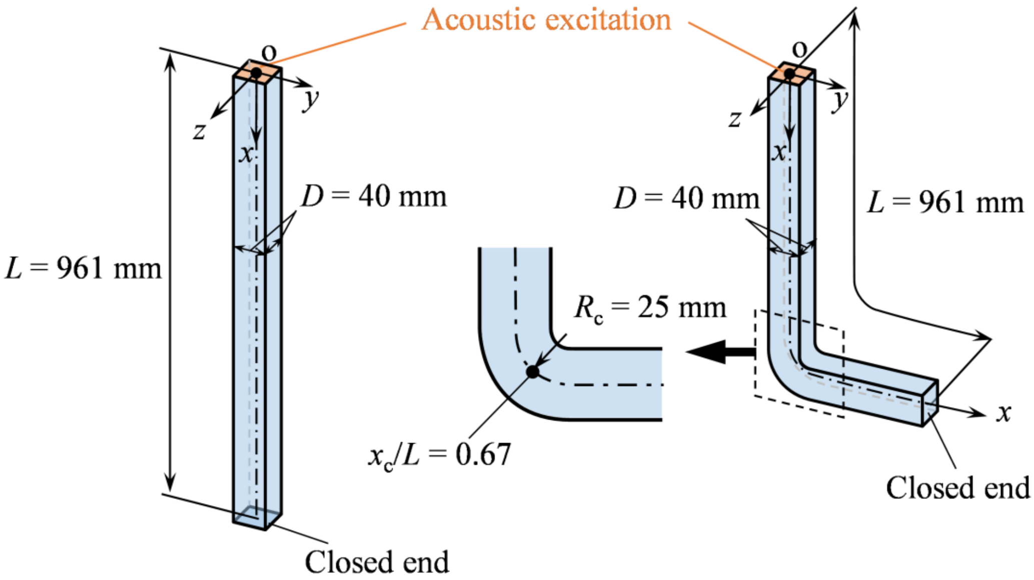

Fig. 1. Configurations of straight and curved ducts with acoustic excitation.

2.2. Control by a plasma actuator

The configurations of the plasma actuator were determined by referring to previous research for the control of aerodynamic noise [14]. As shown in Fig. 2(a), the present plasma actuator consists of 18-µm thick embedded and exposed copper electrodes with a 200-µm thick dielectric polyimide layer sandwiched between the electrodes. The control was performed using a flush-mounted electrode configuration [14,20], which was used to suppress the effects of plasma actuator protrusion from the wall on the flow and energy loss. The streamwise (x-direction) lengths of the exposed and embedded electrodes, which were wide in the spanwise (z) direction, were 1 and 3 mm, respectively. The plasma actuator was installed in the spanwise range of z/D = -0.4 – 0.4. In this range, approximately two-dimensional flow separation occurred in the preliminary computation of the baseline flow, where the effects of the corner vortices between the inner wall of the curvature and the spanwise end walls on the flow were negligibly small. For control by a plasma actuator, hereafter referred to as $N_{PA} = 1$, the exposed electrode of the plasma actuator was located near the curvature in the straight section toward the closed end (closed-end side of the curvature), as shown in Fig. 2(a). Preliminary computations confirmed that the plasma actuator at this position can control the acoustic oscillatory flow around the curvature. Moreover, the computation for the control with two plasma actuators installed near the curvature in the two straight sections toward the open and closed ends (open-end side and closed-end side of the curvature) was conducted, hereafter referred to as $N_{PA} = 2$, as shown in Fig. 2(a).

A schematic of the intermittent driving of the plasma actuator, where the AC voltage is cyclically switched on and off, is shown in Fig. 2(b). The plasma actuator was driven intermittently at the same frequency as the excitation frequency f_a. The waveform of the driving voltage for the intermittent control was shown in Fig. 2(c). The ratio of the actuator-on duration to the intermittent period is called the duty ratio, β, and it was varied from 0.25 to 1.0 for $N_{PA} = 1$. The duty ratio of $\beta = 1.0$ corresponds to continuous control. The power consumption for driving the plasma actuator can be proportionally decreased for the smaller duty ratio. The AC driving voltages were set to $V_{pp} = 9.4$, 18, and 22 kV with a frequency of $f_{PA} = 4.2$ kHz. The conditions of $V_{pp} = 18$ and 22 kV were found to be the relatively effective control conditions for the present acoustic oscillatory flow based on the preliminary computations. The induced volume flow rate by continuously driving the plasma actuator with $V_{pp} = 18$ kV was $Q_{PA}/D^2u_{a,max} = 0.011$ for $Re_a = 4.0\times10^4$. It is noted that the increase of the driving voltage to $V_{pp} = 18$, 22 kV for the present plasma actuator with a 200-μm thick dielectric polyimide layer can possibly lead to the breakdown of the dielectric layer or saturation of the induced velocity [21,22]. The optimization of the arrangement of electrode and dielectric layer and driving conditions such as driving frequency and waveform is necessary to realize the present predicted induced flow in experiments. The experimental validation of the present computational control effects is a future work.

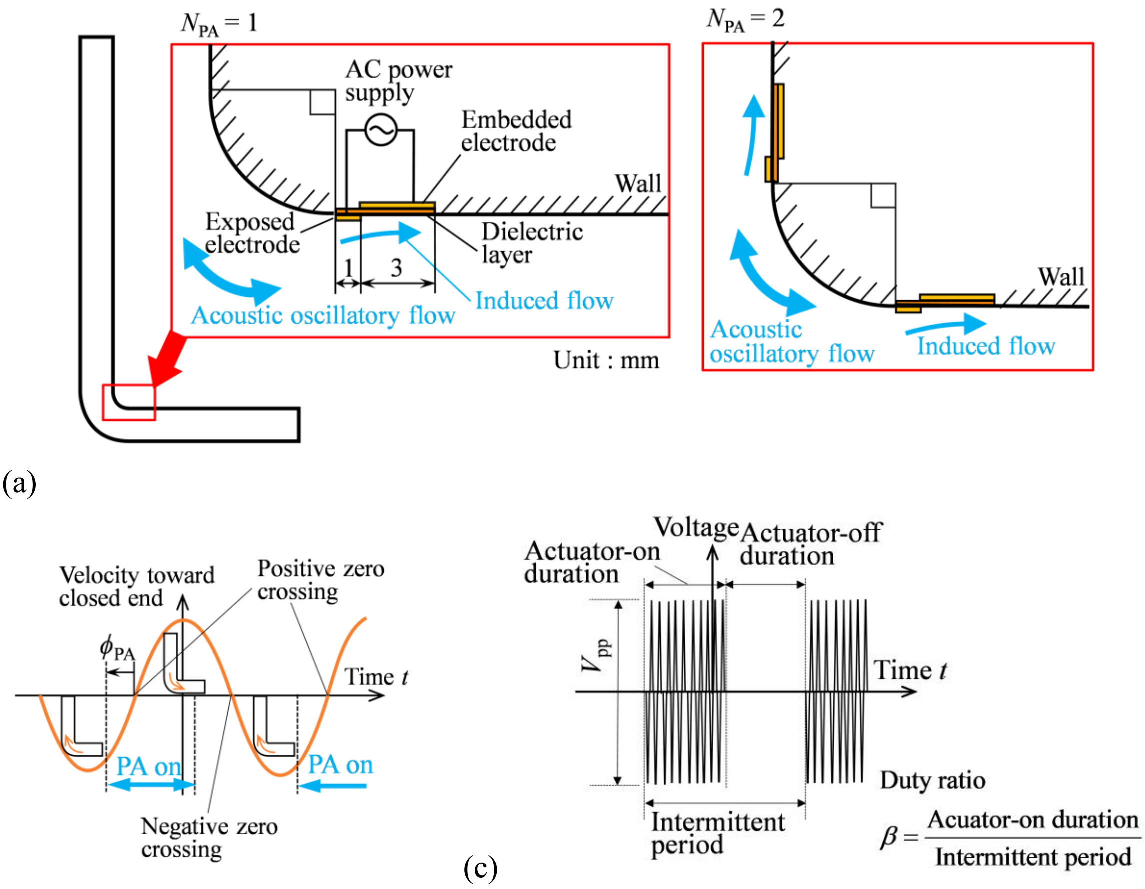

Fig. 2. Control by plasma actuator(s). (a) Arrangement of plasma actuator(s). (b) Schematic of driving the plasma actuator at the closed-end side of the curvature ($N_{PA} = 1$). (c) Waveform of driving voltage for intermittent control.

The phase of the intermittent control, ϕ_{PA}, was varied in the range of $-\pi/2 - \pi/2$ with $\beta = 0.5$ for $N_{PA} = 1$. This phase was defined as the difference between the phase of the switch-on of the plasma actuator and the phase at which the cross-sectional-averaged velocity changed from the negative ($-x$) direction to the positive ($+x$) direction at the curvature (positive zero crossing), as shown in Fig. 2(b). For $N_{PA} = 2$, the two plasma actuators at the closed-end and open-end sides of the curvature were alternately driven with a phase shift corresponding to half of the period, whereas the plasma actuator at the closed-end side was driven with $\phi_{PA} = 0$, $\beta = 0.5$, and V_{PP} = 18 kV.

2.3. Computational methodology

2.3.1. Governing equations and finite-difference scheme

To clarify the acoustic oscillatory flow and acoustic energy loss around the curvature, the flow and acoustic fields were simultaneously simulated by solving the three-dimensional compressible Navier–Stokes equations with the mass, momentum, and energy conservation laws in the following conservation form based on the orthogonal coordinate axes of X, Y, Z, of which directions agree with those of x, y, z axes at the open end of the duct:

$$\mathbf{Q}_t + \left(\mathbf{E} - \mathbf{E}_\mathrm{v}\right)_x + \left(\mathbf{F} - \mathbf{F}_\mathrm{v}\right)_y + \left(\mathbf{G} - \mathbf{G}_\mathrm{v}\right)_z = k\mathbf{D}, \tag{1}$$

$$\mathbf{Q} = (\rho, \rho U, \rho V, \rho W, \rho e)^\mathrm{T}, \tag{2}$$

$$\mathbf{E} = \begin{pmatrix} \rho U \\ p + \rho U^2 \\ \rho UV \\ \rho UW \\ (\rho e + p)U \end{pmatrix}, \mathbf{F} = \begin{pmatrix} \rho V \\ \rho UV \\ p + \rho V^2 \\ \rho VW \\ (\rho e + p)V \end{pmatrix}, \mathbf{G} = \begin{pmatrix} \rho W \\ \rho UW \\ \rho VW \\ p + \rho W^2 \\ (\rho e + p)W \end{pmatrix}, \tag{3}$$

$$k = \begin{cases} \begin{cases} 1 & \left(0 \le \dfrac{\phi_u(t) + \phi_\mathrm{PA}}{2\pi} \le \beta\right) \\ 0 & \left(\beta < \dfrac{\phi_u(t) + \phi_\mathrm{PA}}{2\pi} < 1\right) \end{cases} & \text{for plasma actuator at closed-end side } (N_\mathrm{PA} = 1, 2), \\ \begin{cases} 1 & \left(0 \le \dfrac{\phi_u(t) + \phi_\mathrm{PA}}{2\pi} + 0.5 \le \beta\right) \\ 0 & \left(\beta < \dfrac{\phi_u(t) + \phi_\mathrm{PA}}{2\pi} + 0.5 < 1\right) \end{cases} & \text{for plasma actuator at open-end side } (N_\mathrm{PA} = 2), \end{cases} \tag{4}$$

where $\mathbf{Q}$ is the vector of conserved variables including the Jacobian for the curvilinear coordinate; $\mathbf{E}$, $\mathbf{F}$, and $\mathbf{G}$ are the inviscid flux vectors; $\mathbf{E}_\mathrm{v}$, $\mathbf{F}_\mathrm{v}$, and $\mathbf{G}_\mathrm{v}$ are the viscous flux vectors. In Eqs. (2,3), ρ is the density, e is the energy per unit mass, and U, V, W are the X, Y, and Z-direction components of the velocity vector, respectively. For the curved resonator, the governing equations for the body-fitted coordinate system [23] along the resonator were solved. To reproduce the body force and energy produced by the plasma actuator, $\mathbf{D}$ was included on the right-hand side of Eq. (1). The intensity of the body force was determined based on the driving voltage according to the method by Suzen [24]. The modeling of the body force and energy by the plasma actuator are described in a previous paper (see Appendix) [14]. The coefficient k was introduced to reproduce the intermittent driving with the duty ratio β. The variable ϕ_u means the phase of the cross-sectional-averaged velocity at the curvature at each time step, where $\phi_u = 0$ is the phase for the positive zero crossing. For $N_{\mathrm{PA}} = 2$, the two plasma actuators were alternately driven, with a phase shift corresponding to half of the period.

The spatial derivatives were evaluated using the sixth-order-accurate compact finite-difference scheme (fourth-order-accurate scheme on the boundaries) [25]. Time integration was performed using the third-order accurate Runge–Kutta method.

2.3.2. Computational domain and initial conditions

Figure 3 shows the computational domain with the boundary conditions for the straight and curved ducts. The sinusoidal fluctuations of pressure and velocity were imposed to reproduce the acoustic excitation by a speaker [1,15,16]. The velocity amplitude on the open end was given by Eqs. (3–5) referring to the analytical solutions [26].

$$u_{\mathrm{a}}\left(y,z\right) = \frac{1-f_v}{1-\chi_v} u_{\mathrm{a,i}}, \tag{5}$$

$$f_v\left(y,z\right) = \frac{\cosh\left((1+i)\dfrac{\max\left(|y|,|z|\right)}{\delta_v}\right)}{\cosh\left((1+i)\dfrac{D}{2\delta_v}\right)}, \tag{6}$$

$$\chi_v = \frac{\tanh\left((1+i)\dfrac{D}{2\delta_v}\right)}{(1+i)\dfrac{D}{2\delta_v}}, \tag{7}$$

where $\delta_{\mathrm{v}} = (2\nu/\omega)^{1/2}$ is the viscous boundary layer thickness of the oscillatory flow. The uniform pressure amplitude of $p_{\mathrm{a}}(y, z) = p_{\mathrm{a,i}}$ was given on the open end. The amplitudes of $u_{\mathrm{a,i}}$ and $p_{\mathrm{a,i}}$ and the phase difference between the pressure and velocity fluctuations on the open end were adjusted so that the amplitude of the pressure fluctuations at the closed end was set as the value, as mentioned in Section 2.1. The details of the boundary conditions for the acoustic excitation were described in a previous paper, where the present boundary condition was confirmed to be appropriate by the comparison of the predicted distributions of the acoustic intensity in the resonator with and without a stack with those measured [15]. On the closed-end and side walls of the duct, non-slip and iso-thermal conditions were imposed.

Regarding the computational grid, 533 and 558 grid points were used in the x-direction for the straight and curved ducts, respectively. The maximum grid spacing in the x-direction was $\Delta x_{\max}/D = 0.05$, which was sufficiently fine to capture the acoustic propagation with wavelengths of $\lambda/D = 32$ and 31 for the straight and curved ducts, respectively. Moreover, the computational grids were sufficiently fine to reproduce the oscillatory viscous boundary layer near the duct wall, with a thickness of $\delta_{\mathrm{v}}/D \equiv (\nu/\pi f_{\mathrm{a}})^{1/2}/D = 3.4\times10^{-3}$. The minimum grid resolution near the wall was $\Delta y_{\min}/D, \Delta z_{\min}/D = 1.7\times10^{-4}$, and the number of grid points in the cross-section was 165×165 points. The total grid points were 14.5 million and 15.2 million for the straight and curved ducts, respectively.

The quiescent flow field was assigned as the initial condition for the computation of the baseline flow. The computational time step was $\Delta t = 7.8\times10^{-9}$ s. The number of time steps for one time period for the excitation frequency, T, was 4.8×10^{5} and 4.6×10^{5} steps for the straight and curved ducts, respectively. The acoustic and flow fields were evaluated based on the computational results after the flow development to periodic flow fields in three periods corresponding to 1.4 million steps from the initial field. The developed baseline flow field was used as the initial flow field for the computation of the controlled flow.

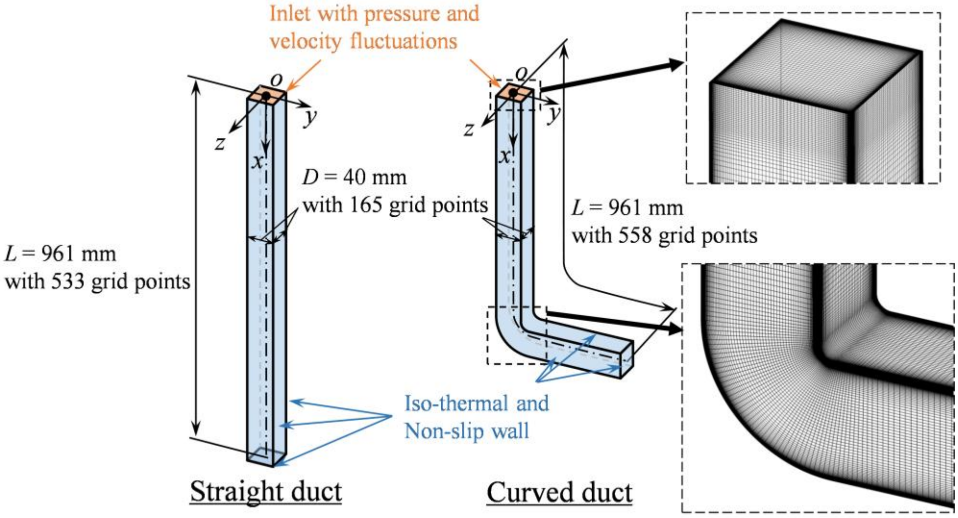

Fig. 3. Computational domain with boundary conditions for straight and curved ducts, where computational grids around open end and curvature are also shown.

2.4. Computational validation

2.4.1. Effects of grid resolution

The computational results obtained with the present grid were compared with those determined using twice grid points in the cross-section for the acoustic oscillatory flow with $Re_a = 3\times10^4$ in the curved duct without control (baseline flow). Figure 4 shows the distributions of the acoustic intensity predicted with the present grid and those with a finer grid. The acoustic intensity was defined using Eq. (8).

$$I = f_a \int_0^{1/f_a} p_{ave}(t) u_{ave}(t)\, dt , \qquad (8)$$

where $p_{ave}(t)$ and $u_{ave}(t)$ are the fluctuations of the cross-sectionally averaged pressure and velocity at the excitation frequency, respectively. As shown in Fig. 4, the acoustic intensity predicted with the present grid was in good agreement with that predicted with the finer grid. This indicates that the fineness of the present grid resolution was sufficient to reproduce the present acoustic oscillatory flow. Detailed discussions of the distributions of acoustic intensity in the duct are described in Section 3.1.1.

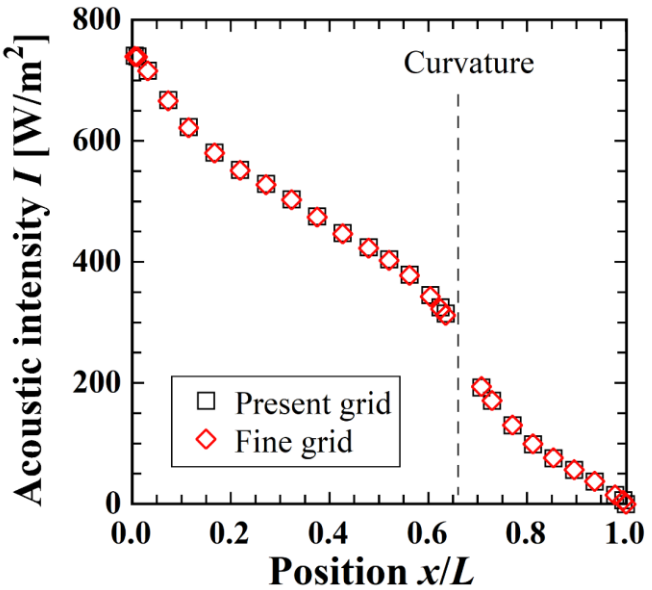

Fig. 4. Distributions of acoustic intensity for baseline acoustic intensity in the curved duct ($\mathrm{Re_a} = 3\times10^4$) predicted with present and finer computational grids, where a dashed line indicates the position of curvature of $x = x_c$.

2.4.2. Comparison of predicted and measured induced flow field by plasma actuator

Figure 5(a) shows the predicted mean velocity profile of the flow induced by the plasma actuator at a position 16 mm from the exposed electrode toward the closed end in the curved duct, along with the measured profile. The plasma actuator was continuously driven by the AC voltage, with a driving voltage of $V_{\mathrm{pp}} = 9.4$ kV in quiescent air without acoustic excitation. The predicted result was compared with that measured using a hot-wire anemometer; here, the experimental methods for driving the plasma actuator and the velocity measurements were the same as those employed in previous research [14]. The above-mentioned driving voltage corresponded to the maximum value for the present driving unit of the plasma actuator (PSI-PGI1040F, KI tech Co., Ltd., Tokyo). The time-series velocity measured by the hot-wire anemometer in the experiment was represented in the computation as $u_{\mathrm{h}} = (u^2 + v^2)^{0.5}$, which corresponded to the velocity component normal to the hot wire placed along the spanwise direction, and the time-averaged value, U_{h}, was predicted. As shown in Fig. 5, both the predicted and measured velocity distributions have a maximum value of approximately 0.7 m/s at a height of 0.5 mm from the duct wall of $y = 20$ mm. Although a discrepancy between the predicted and measured values appears due to the difficulties in accurate measurements for small velocities far from the wall, the predicted profile almost entirely agrees with the measured one, particularly around the maximum velocity.

Figure 5(b) shows the predicted profiles of the velocity difference between the baseline and controlled flows ($V_{\mathrm{pp}} = 18, 22$ kV, $\beta = 0.5$, $\phi_{\mathrm{PA}} = 0$) at the time of the maximum cross-sectional-averaged velocity toward the closed end for $\mathrm{Re_a} = 4.0\times10^4$. The maximum increase of velocity near the wall of 6 m/s and 10 m/s was predicted by driving the plasma actuator with $V_{\mathrm{pp}} = 18$, 22 kV, respectively. As discussed in Sec. 3, the control with $V_{\mathrm{pp}} = 18$ kV was shown to reduce the loss of acoustic intensity around the curvature in the resonator. In the literature [27], the maximum velocity of 7 m/s, which is higher than the present induced velocity by V_{pp} = 18 kV, was obtained by a plasma actuator. Therefore, the proposed control by the plasma actuator is expected to be realized in actual experiments with appropriate power supply device, arrangements of electrode and dielectric layer, and driving conditions.

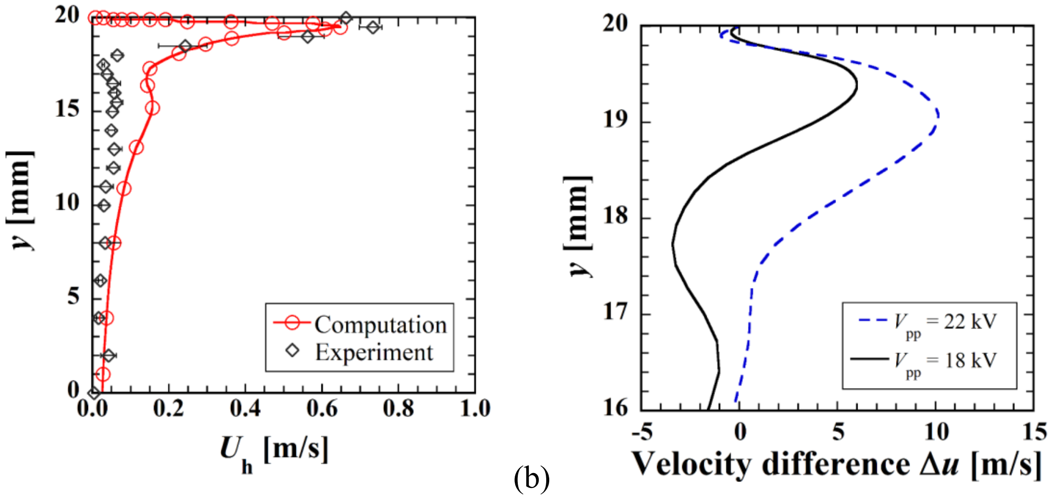

(a) (b)

Fig. 5. Velocity profiles of induced flow by a plasma actuator at a position 16 mm from the exposed electrode toward the closed end in the curved duct. (a) Mean predicted and measured velocity profiles of induced flow by a continuously driven plasma actuator for V_{pp} = 9.4 kV without acoustic excitation, where the variations of measured mean data for the time durations of computations (20 ms) were shown with bars. (b) Velocity difference between the baseline and controlled flows (V_{pp} = 18, 22 kV, β = 0.5, ϕ_{PA} = 0) at the time of the maximum cross-sectional-averaged velocity toward the closed end for $Re_a = 4.0\times10^4$.

3. Result and Discussion

3.1. Baseline flow

3.1.1. Acoustic intensity

Figure 6 shows the predicted variations in the acoustic intensity in the straight and curved ducts for $Re_a = 4\times10^4$, with the theoretical curve for the straight duct obtained using the linear theory [15,28]. The acoustic intensities for both ducts are shown to decrease to zero at a position closer to the closed end because of the viscous dissipation and the thermal conduction around the wall. The distributions predicted for the straight duct are approximately along the theoretical curve, while a discrepancy occurs owing to the occurrence of nonlinear effects due to the large amplitude of the velocity fluctuations around $x/L = 0$ and 0.6. The decrease in the predicted acoustic intensity (acoustic intensity loss) at approximately $x/L = 0.67$, which corresponds to the installation position of the curvature x_c, becomes particularly sharp for the curved duct. This indicates the generation of acoustic power loss owing to the curvature. The slope is slightly sharper at this position than at the other positions, even for the straight duct. This is because this position corresponds to the antinode of the velocity fluctuations in the acoustic mode and the acoustic power loss increases. The difference in the acoustic intensity between $x/L = 0$ and 1.0 indicates the acoustic power loss across the entire duct. Figure 6 shows that the acoustic power loss in the curved duct is larger than that in the straight duct.

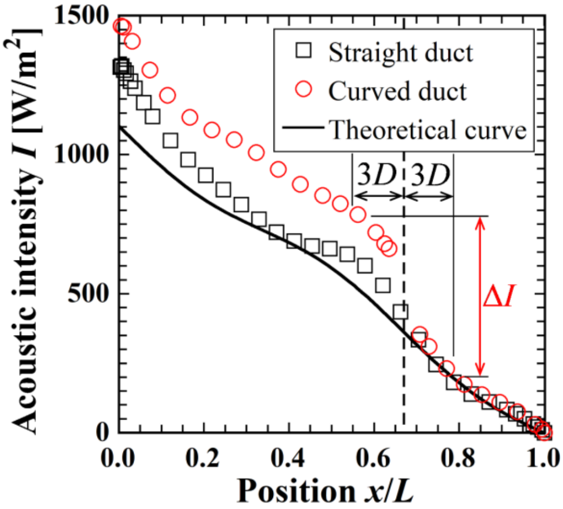

Fig. 6. Predicted variations of acoustic intensity in straight and curved ducts ($Re_a = 4.0 \times 10^4$), where a dashed line indicates the position of curvature of $x = x_c$.

The acoustic intensity loss around $x = x_c$ was evaluated based on the difference between the upstream acoustic intensity I_u and the downstream acoustic intensity I_d as shown in Eq. (9).

$$\Delta I = I_u - I_d \,. \tag{9}$$

Here, I_u and I_d were evaluated at the points x_c-3D and x_c+3D, respectively, where the direct effects of the curvature on the slope of the acoustic intensity were negligibly small for the curved duct. Figure 7 shows the predicted variations of the baseline acoustic intensity loss ΔI around $x = x_c$ with varying acoustic Reynolds number, Re_a, along with the preliminary experimental results and the linear theoretical curve for the straight duct [28]. The experimental data acquired with a two-sensor method [29,30] using the experimental setup described in the previous paper [15] are shown with the variation of multiple experimental data at $Re_a = 2.7\times10^4$. As shown in Fig. 7(a), the measured data are almost along the predicted distributions, confirming the validity of the computational accuracy. Figure 7(b) shows the predicted acoustic intensity losses at $Re_a = 3.0\times10^4$ for straight and curved ducts were shown with the measured data. The measured values at $Re_a = 3.0\times10^4$ were estimated using the existing measured data at the Reynolds number closest to $Re_a = 3.0\times10^4$ based on the curve of the predicted values. Although the reason for the variation of experimental data in multiple tests is currently unclear, the predicted value is in the experimental variation as shown in Fig. 7(b). Moreover, Fig. 7(a) shows that the predicted distributions of the acoustic intensity for the straight curve are approximately along the theoretical curve, where the acoustic power loss increases with the acoustic Reynolds number. The acoustic intensity loss for the curved duct becomes larger than that of the straight curve, particularly at a high Reynolds number of $Re_a \geq 3.0\times10^4$. This is related to the change in acoustic oscillatory flow around the curvature with the acoustic Reynolds number, as discussed in the next section.

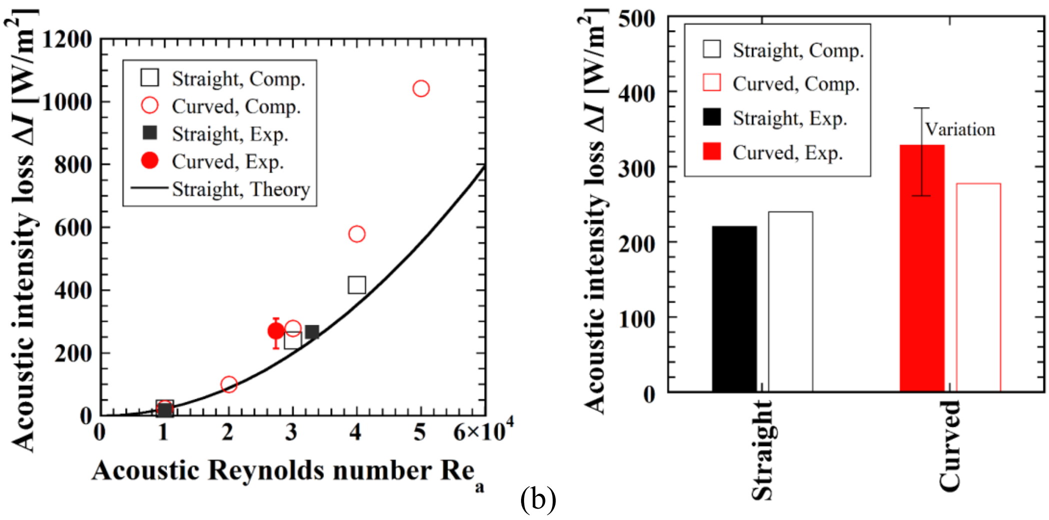

(a) (b)

Fig. 7. Predicted acoustic intensity loss compared with preliminarily measured values and a theoretical curve [15,28], where the variation for experimental data at $\mathrm{Re_a} = 2.7\times10^4$ is represented by an error bar. (a) Variations of baseline predicted acoustic intensity loss with acoustic Reynolds number. (b) Acoustic intensity losses at $\mathrm{Re_a} = 3.0\times10^4$, where the measured values are estimated by the existing measured loss at the Reynolds number closest to $\mathrm{Re_a} = 3.0\times10^4$ and the curve of predicted values.

3.1.2. Acoustic oscillatory flow around a curvature

Figure 8 shows the predicted instantaneous velocity vectors and contours of the velocity magnitude in the *x*-*y* cross-section ($z = 0$) around the curvature in the curved duct at $\mathrm{Re_a} = 1.0\times10^4$ and 4.0×10^4. The results at different times are shown, where $tf_a = 0$ and 0.5 are the times of the maximum cross-sectional-averaged velocity toward the closed and open ends at the curvature, respectively. As shown in Fig. 8(a), for $\mathrm{Re_a} = 1.0\times10^4$, the velocity magnitude becomes larger around the inner wall of the curvature at both times, while no flow separation is observed. Conversely, as shown in Fig. 8(b) for $\mathrm{Re_a} = 4.0\times10^4$, flow separation occurs at the closed and open ends of the curvature at $tf_a = 0$ and 0.5, respectively. At $tf_a = 0.25$, a vortex is observed at the closed-end side of the curvature with a negative zero crossing of the cross-sectional averaged velocity at the curvature. Moreover, a similar vortex is observed at the open-end side of the curvature, with a positive zero crossing of the cross-sectional averaged velocity at $tf_a = 0.75$. These flow separations and vortices lead to an increase in the acoustic power loss for the curved duct, as shown in Fig. 7.

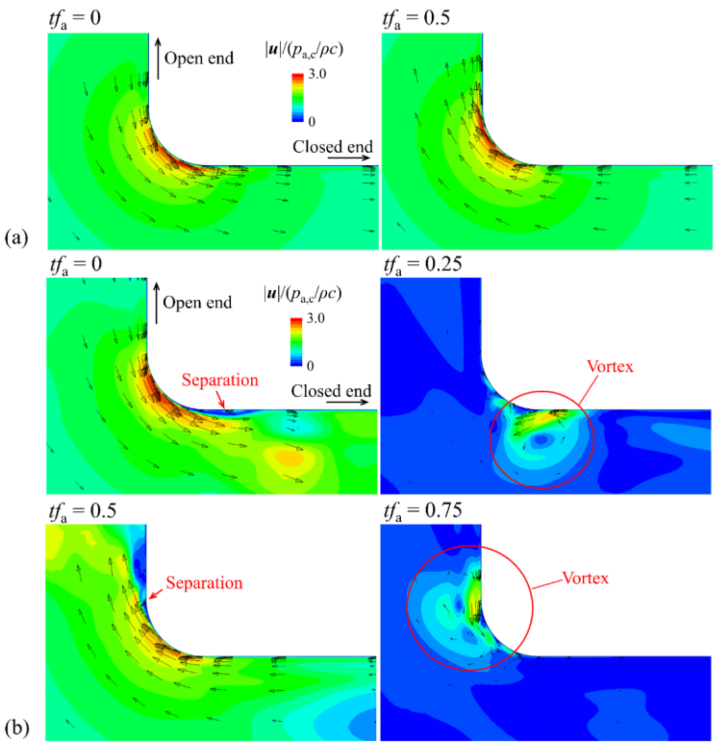

Fig. 8. Baseline instantaneous velocity vectors and contours of velocity magnitude around the curvature in a curved duct ($z = 0$). (a) $\mathrm{Re_a} = 1.0\times10^4$. (b) $\mathrm{Re_a} = 4.0\times10^4$.

3.2. Control effects by a plasma actuator in a curved duct

3.2.1. Control effects on acoustic intensity

Figure 9 shows the controlled distributions of acoustic intensity in the curved duct for $\mathrm{Re_a} = 4.0\times10^4$ with the baseline distribution. The results of the control of $N_{\mathrm{PA}} = 1$ ($V_{\mathrm{pp}} = 18$ and 22 kV) and $N_{\mathrm{PA}} = 2$ ($V_{\mathrm{pp}} = 18$ kV) under the condition of intermittent control of $\beta = 0.5$ and $\phi_{\mathrm{PA}} = 0$. As shown in Fig. 9, the acoustic intensity loss at the curvature was reduced by all controls compared with the baseline condition. The lowering of the acoustic intensity before the curve indicates that necessary acoustic intensity given to the resonator for the constant pressure amplitude at the closed end ($p_{a,c} = 6.2$ kPa in this case) can be reduced by the suppression of acoustic intensity loss due to the curvature. This means that larger acoustic power can be utilized for heat transport in a thermoacoustic heat pump [1,15,16]. A larger reduction in the acoustic intensity loss due to the curvature was achieved with a higher driving voltage and a greater number of driven plasma actuators compared to the control conditions of $N_{\mathrm{PA}} = 1$ and

V_{PP} = 18 kV. Meanwhile, it is noted that the power consumption for the control also increases with an increase in the driving voltage and the number of plasma actuators.

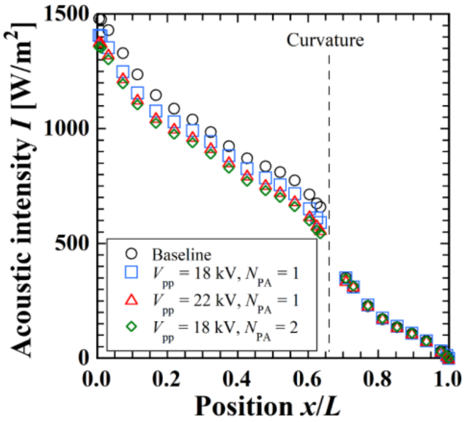

Fig. 9. Distributions of controlled acoustic intensity in a curved duct ($Re_a = 4.0\times10^4$) with three control conditions of $N_{PA} = 1$ (V_{pp} = 18, 22 kV) and $N_{PA} = 2$ (V_{PP} = 18 kV) under the condition of intermittent control of $\beta = 0.5$ and $\phi_{PA} = 0$ compared with the baseline distribution.

Based on existing literature [14,21,31], the power consumption of a plasma actuator is assumed to increase in proportion to $V_{PP}^{3.5}$. To evaluate the control efficiency considering the power consumption, the reduction in the acoustic intensity loss, $\Delta I_{off} - \Delta I_{on}$, divided by the product of the number of plasma actuators, N_{PA}, and the driving voltage ratio to the power of 3.5, $(V_{pp}/V_{pp,ref})^{3.5}$, where the reference driving voltage is $V_{pp,ref}$ = 18 kV, was calculated. The power consumption for V_{pp} = 18 kV and $\beta = 0.5$ was estimated to be about 6 W referring to the previous research [14]. Figure 10 shows the calculated results for the three control conditions for $\beta = 0.5$, where the vertical axis indicates the estimated acoustic intensity loss with each control condition on the assumption of usage of the same power consumption with that of N_{PA} = 1 and V_{pp} = 18 kV. The control with $N_{PA} = 1$ and V_{pp} = 18 kV achieved the highest normalized reduction in the acoustic intensity loss based on the power consumption, which indicates the ability of the most efficient control. The reduction of the acoustic power loss with $N_{PA} = 1$ and V_{pp} = 18 kV was $(\Delta I_{off} - \Delta I_{on})D^2 = 0.1$ W, which was smaller than the power consumption of the plasma actuator. The suppression of the power consumption of the plasma actuator by optimizing the driving conditions and electrode arrangement is a future problem for practical application of this control method. In this paper, the mechanism for the reduction of the acoustic intensity loss by the plasma actuator is clarified as the first step. In the following sections, the control effects for N_{PA} = 1 and V_{pp} = 18 kV are discussed.

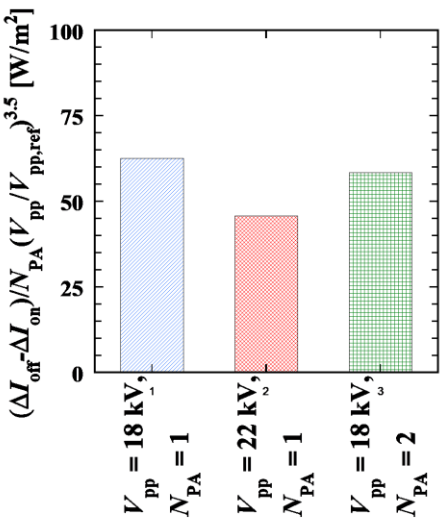

Fig. 10. Reduction of the acoustic intensity loss for $\mathrm{Re_a} = 4.0\times10^4$ by control, $\Delta I_{\mathrm{off}} - \Delta I_{\mathrm{on}}$, divided by the product of the number of plasma actuators (N_{PA}) and $(V_{pp}/V_{pp,ref})^{3.5}$, where the reference driving voltage is $V_{pp,ref}$ = 18 kV, for three control conditions of N_{PA} = 1 (V_{pp} = 18, 22 kV) and N_{PA} = 2 (V_{PP} = 18 kV) under the intermittent control condition of β = 0.5 and ϕ_{PA} = 0.

3.2.2. Controlled acoustic oscillatory flow around curvature

Figure 11 shows the predicted instantaneous velocity vectors and contours of the velocity magnitude around the curvature at $\mathrm{Re_a} = 4.0\times10^4$ under the control of V_{pp} = 18 kV, N_{PA} = 1, β = 0.5, and ϕ_{PA} = 0. In the baseline flow field shown in Fig. 8(b), flow separation occurred near the closed-end side of the curvature at tf_a = 0. By contrast, flow separation was suppressed at tf_a = 0 in the controlled flow, as shown in Fig. 11. This is because the reverse flow near the wall was suppressed by the flow induced by the plasma actuator. As a result, the vortex observed in the baseline flow field at tf_a = 0.25 in Fig. 8(b), which is generated owing to the occurrence of the flow separation, is also suppressed by the control in Fig. 11. Moreover, despite the lack of direct control at the open-end side, the flow separation region near the open-end side of the curvature at tf_a = 0.5 also becomes smaller owing to the control. In the baseline flow, the vortex with counterclockwise rotation at the closed-end side of the curvature at tf_a =

0.25 was advected toward the open end by the negative acoustic particle velocity, where the momentum of the vortex in the -y direction promotes the flow separating from the wall at the open-end side of the curvature at $tf_a = 0.5$ in Fig. 8(b). For the controlled flow, the suppression of the vortex at the closed-end side of the curvature leads to the suppression of flow separation at the open-end side of the curvature. Therefore, control with one plasma actuator installed at the closed-end side of the curvature ($N_{PA} = 1$) resulted in the suppression of the flow separation region over the entire period.

In the past research for the suppression of flow separation around a body with a kink shape in a unidirectional freestream [32], the flow separation was effectively suppressed with a plasma actuator installed close to the point of the flow separation. As shown in Fig. 8(b) (tf_a = 0), the region of flow separation particularly begins to become large near the curvature in the straight section toward the closed end. This position corresponds to that for the present installation of the plasma actuator. Although the installation of the plasma actuator on the curvature upstream of the flow separation point can be more effective, the present installation position on the straight section is suitable considering experimental installation of the plasma actuator to a curved resonator.

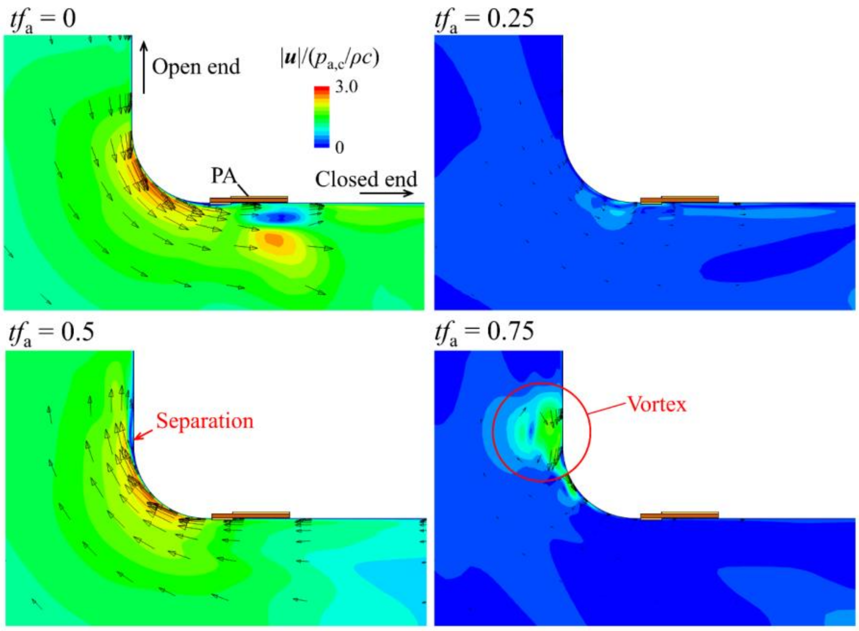

Fig. 11. Controlled instantaneous velocity vectors and contours of velocity magnitude around curvature ($z = 0$) with the control condition of $V_{pp} = 18$ kV, $N_{PA} = 1$, $\beta = 0.5$ and $\phi_{PA} = 0$ for $Re_a = 4.0\times10^4$.

Figure 12 shows the three-dimensional distributions of vortices at $tf_a = 0.25$ for $Re_a = 4\times10^4$ by the iso-surfaces of the second invariant of the velocity gradient tensor based on the orthogonal coordinate axes of X, Y, Z. It is shown that the vortices related to flow separation around the inner wall of the curvature become weaker by the control in almost all spanwise positions. Meanwhile, the vortices in the limited region near the corner between the spanwise end wall and the inner wall of the curvature remain in the present controlled flow, and the control of these vortices is a topic for future work. The suppression of the vortices related to flow separation leads to a reduction in the energy dissipation in the flow, as discussed in the next paragraph.

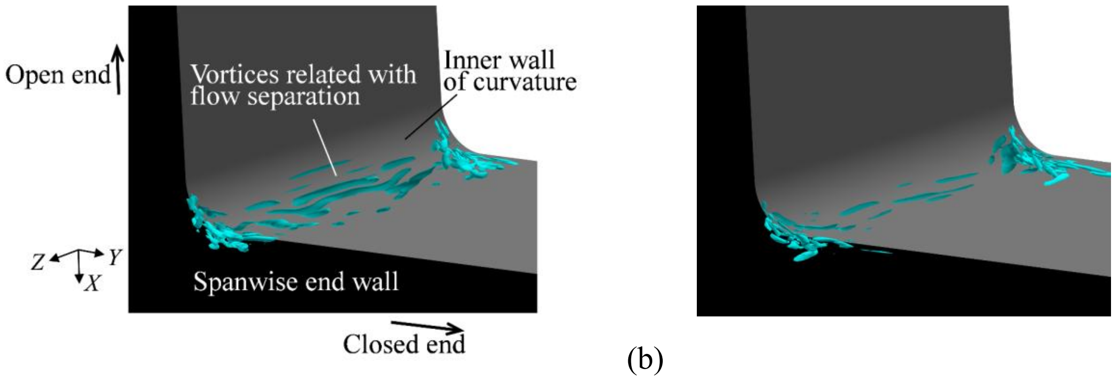

(a) (b)

Fig. 12. Iso-surfaces of second invariant, $q/(u_a/\delta_v)^2 = 100$, for acoustic oscillatory flow around the curvature at $tf_a = 0.25$ for $Re_a = 4.0\times10^4$. (a) Baseline flow. (b) Controlled flow with $V_{pp} = 18$ kV, $N_{PA} = 1$, $\beta = 0.5$, and $\phi_{PA} = 0$.

To evaluate the energy loss based on the flow field, the value of the viscous dissipation function Φ around the curvature in the baseline and controlled flows was calculated using Eq. (10) [33].

$$\Phi = \mu\left[\left\{\left(\frac{\partial V}{\partial X}+\frac{\partial W}{\partial Y}\right)^2+\left(\frac{\partial W}{\partial X}+\frac{\partial U}{\partial Z}\right)^2+\left(\frac{\partial U}{\partial Y}+\frac{\partial V}{\partial X}\right)^2\right\}\right.$$
$$\left.+\frac{2}{3}\left\{\left(\frac{\partial V}{\partial Y}-\frac{\partial W}{\partial Z}\right)^2+\left(\frac{\partial W}{\partial Z}-\frac{\partial U}{\partial X}\right)^2+\left(\frac{\partial U}{\partial X}-\frac{\partial V}{\partial Y}\right)^2\right\}\right], \quad (10)$$

where μ is the viscosity coefficient. Figure 13 shows the baseline and controlled contours of the dissipation function at $tf_a = 0.25$ for $Re_a = 4\times10^4$. In the baseline flow in Fig. 13 (a), the value of the dissipation function becomes large in the region of the vortex formation observed at $tf_a = 0.25$, as shown in Figs. 8(b) and 12(a). This confirms that the amount of energy dissipated owing to viscosity is increased by vortex formation caused by flow separation. In the controlled flow in Fig. 13(b), the region with a large value of the dissipation function becomes smaller compared with the baseline flow owing to the suppression of vortex generation at the closed-end side of the curvature. This leads to a reduction in the acoustic power loss around the curvature by control, as shown in Fig. 9.

(a) 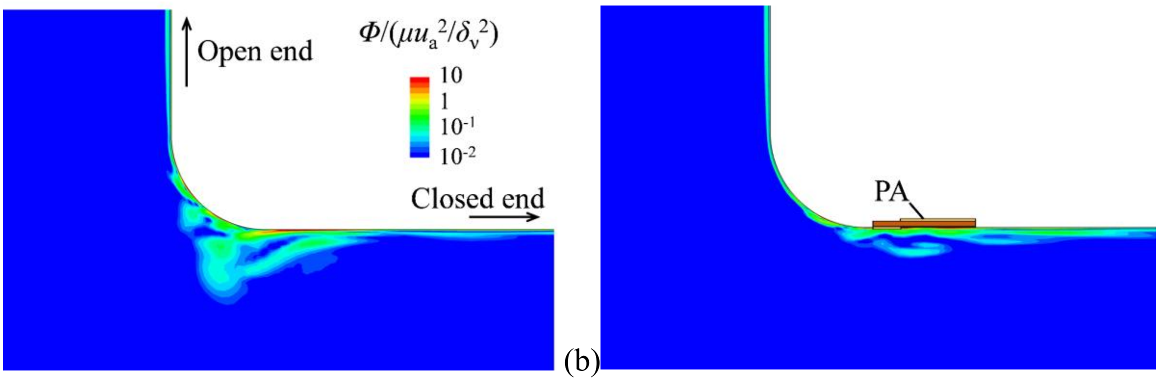

Fig. 13. Instantaneous contours of the values of the dissipation function ($z = 0$) with logarithmic color variation at $tf_a = 0.25$ for $Re_a = 4.0\times10^4$. (a) Baseline flow. (b) Controlled flow with V_{pp} = 18 kV, $N_{PA} = 1$, $\beta = 0.5$, and $\phi_{PA} = 0$.

3.2.3. Effective conditions of intermittent control

To evaluate the control effects on acoustic power loss, the loss reduction ratio R is defined as follows:

$$R = \frac{\Delta I_{off} - \Delta I_{on}}{\Delta I_{off} - \Delta I_{st}}, \quad (11)$$

where ΔI_{st} is the acoustic intensity loss in a straight duct calculated using Eq. (9). The loss reduction ratio R is the ratio of the reduction in acoustic power loss by the control to the baseline acoustic power loss generated by the curvature. Figure 14 shows the variation in the loss reduction ratio R with the phase of the intermittent control with V_{pp} = 18 kV, N_{PA} = 1, and β = 0.5 for the acoustic oscillatory flow in the curved duct with $Re_a = 4.0\times10^4$. The control in the range of ϕ_{PA} = -π/6 – 0 is shown to reduce the acoustic intensity loss more effectively around the curvature, where the maximum loss reduction ratio of R = 0.46 is achieved with the phase ϕ_{PA} = 0.

Figure 15 shows the baseline and controlled instantaneous velocity profiles (tf_a = 0.25) at a position 1 mm away from the curvature in the straight section toward the closed end, where the flow separation with vortex generation appears, as shown in Fig. 8(b). As shown in Fig. 15, the region for the reverse flow is spread because of the vortex near the wall from tf_a = 0 to 0.25 in the baseline flow. The reverse flow also appears in the controlled flow with ϕ_{PA} = π/2 because the control switches off at t = 0, and flow separation is generated after t = 0. Meanwhile, the reverse flow was more effectively suppressed by control with ϕ_{PA} = -π/6, 0. This implies that the plasma actuator must be driven until the time for the negative zero crossing of the cross-sectional-averaged velocity for effective control.

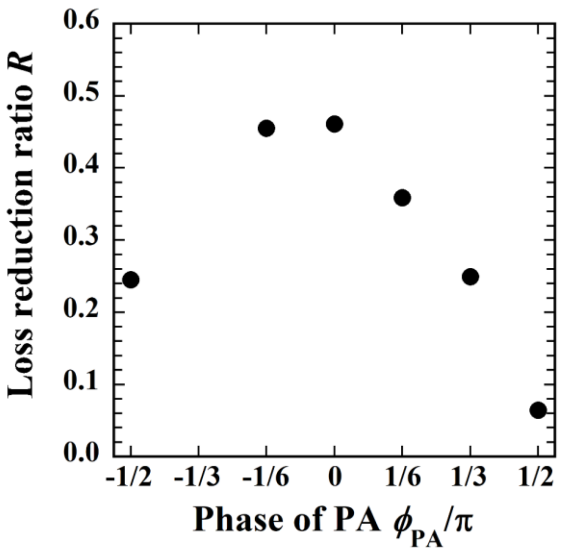

Fig. 14. Variation of loss reduction ratio R with phase of intermittent control (V_{pp} = 18 kV, N_{PA} = 1, β = 0.5) for $Re_a = 4.0\times10^4$.

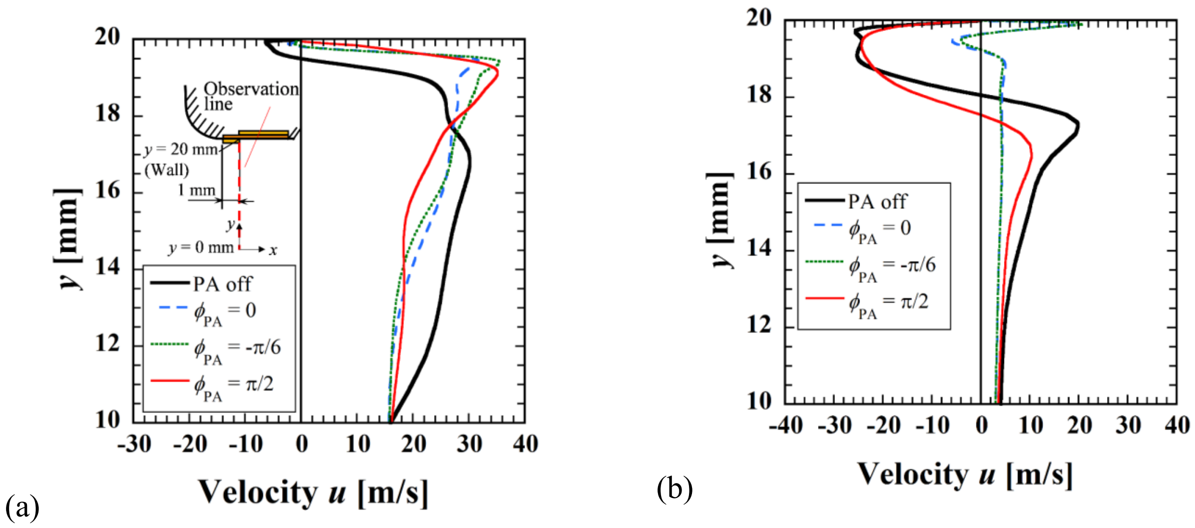

Fig. 15. Controlled velocity profiles at position 1 mm from the curvature in the straight section toward the closed end (V_{pp} = 18 kV, N_{PA} = 1, β = 0.5) compared with the baseline flow for $Re_a = 4.0\times10^4$. (a) tf_a = 0. (b) tf_a = 0.25.

Figure 16 shows the variation in the control effects on the acoustic intensity loss with the duty ratio of the intermittent control (V_{pp} = 18 kV, N_{PA} = 1, ϕ_{PA} = 0) for an acoustic oscillatory flow with $Re_a = 4\times10^4$. The reduction in the acoustic intensity loss divided by the duty ratio $(\Delta I_{off} - \Delta I_{on})/\beta$ is shown to evaluate the control effects normalized based on the power consumption of the plasma actuator. As shown in Fig. 16, the highest normalized control effects are achieved by the control with β = 0.5. In the control with a smaller duty ratio of β = 0.25, the plasma actuator is switched off at t = 0 with the maximum cross-sectional-averaged velocity toward the closed end. Consequently, the flow separation after t = 0 cannot be suppressed, as in the control with $\phi_{PA} = \pi/2$ (β = 0.5), as shown in Fig. 15(b). For larger duty ratios of β = 0.75, 1.0, (continuous), the plasma actuator is driven in the time duration of tf_a = 0.5 – 1.0, when no intense flow separation occurs at the closed-end side of the curvature. This leads to the deterioration of the control effects, normalized based on power consumption (control efficiency). Therefore, the acoustic intensity loss was most efficiently reduced by control with β = 0.5. Based on the present results, it is summarized that the effective condition of the intermittent control with appropriate efficiency in this research is $\beta = 0.5$ and $\phi_{PA} = -\pi/6–0$ ($V_{pp} = 18$ kV, $N_{PA} = 1$).

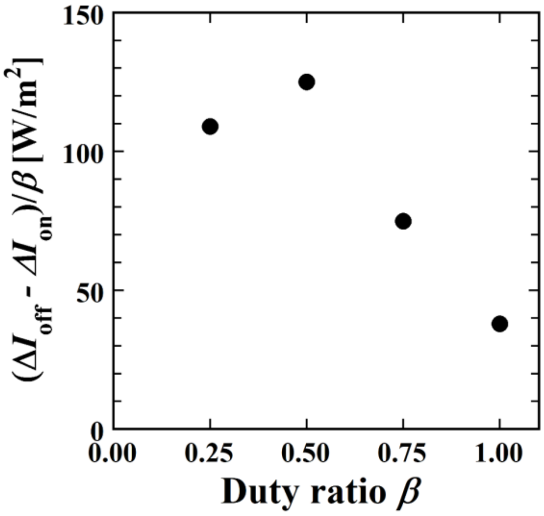

Fig. 16. Variation of the control effects on the acoustic intensity loss normalized based on the power consumption of the plasma actuator with the duty ratio ($V_{pp} = 18$ kV, $N_{PA} = 1$, $\phi_{PA} = 0$), where the reduction of acoustic intensity divided by the duty ratio is shown, for the acoustic oscillatory flow in the curved duct with $Re_a = 4.0\times10^4$.

4. Conclusion

Compressible flow simulations for the control of acoustic oscillatory flows in a curved duct using a plasma actuator were conducted to clarify control methods for reducing the acoustic energy loss around a curvature. In the baseline flow, the loss of the acoustic power in the curved duct became larger compared with that in a straight duct, particularly with a high acoustic Reynolds number of $Re_a \geq 3\times10^4$, where flow separation and vortex formation periodically occurred around the inner wall of the curvature. The suppression of the flow separation by an intermittently driven plasma actuator, which was installed at the closed-end side of the curvature, successfully led to a reduction in acoustic power loss through the suppression of viscous energy dissipation. Moreover, it was discovered that driving the plasma actuator only at one (closed-end) side of the curvature could suppress the flow separation at the other (open-end) side of the curvature. Consequently, this was found to lead to efficient control by considering the power consumption of the plasma actuator. The phase of the efficient intermittent control with a duty ratio of 0.5 was identified to be $-\pi/6 – 0$ with reference to the cross-sectional-averaged velocity fluctuations around the curvature. This implies that relatively effective control must drive the plasma actuator during the time duration until the time for the negative zero crossing of the cross-sectional-averaged velocity. As a result of this control, the reverse flow near the wall owing to the flow separation and vortex formation in the baseline flow was suppressed. However, the power consumption of the plasma actuator was still larger than the loss reduction of acoustic power, and the improvement of control efficiency is necessary for the actual application of the plasma actuator. An experimental study is also a future task to demonstrate the effectiveness of the plasma actuator. However, intermittent active flow control on the minor loss that can occur in machinery related to sound, such as thermoacoustic devices, was quantitatively evaluated for the first time in the present research. Moreover, it is beneficial for the design of these devices to obtain knowledge regarding the relationship between flow separation and vortex generation and the minor loss in the acoustic oscillatory flow through flow control.

Acknowledgements

This work was partly supported by JSPS KAKENHI Grant Number 21K03874, MEXT as “Program for Promoting Researches on the Supercomputer Fugaku” (hp210174). The authors also express their gratitude for the experimental cooperation of Mr. Fujisawa and Mr. Ulziibuyan.

Appendix Modeling of body force by plasma actuator

The modeling of the body force and energy by the plasma actuator is explained herein. The details are already described in a previous paper [34]. The body force and energy produced by the plasma actuator, **D**, in Eq. (1) were evaluated as follows:

$$\mathbf{D} = \begin{pmatrix} 0 \\ S_x \\ S_y \\ S_z \\ S_x u + S_y v + S_z w \end{pmatrix}, \tag{A1}$$

$$\begin{pmatrix} S_x \\ S_y \\ S_z \end{pmatrix} = A \sin^2\left(2\pi f_{\mathrm{PA}} t\right) \rho_{\mathrm{c}} \left(-\nabla \phi\right), \tag{A2}$$

$$A = \begin{cases} 1.0 & (\sin(2\pi f_{\mathrm{PA}} t) \le 0) \\ -0.4 & (\sin(2\pi f_{\mathrm{PA}} t) > 0) \end{cases}. \tag{A3}$$

In Eq. (A1), u, v, and w are the velocity components in the x-, y-, and z-directions, respectively; ρ_{c} is the plasma density, and ϕ_k is the electric potential. The plasma density and electric potential distributions were computed referring to the literatures [24]. The square of the sine function in Eq. (A2) indicates that the plasma discharge occurs twice in one period, similar to the body-force model of Kaneda *et al*. [35]. Coefficient A was introduced to represent the change in the magnitude and direction of the body forces between the positive and negative applied voltages.

References

[1] Swift GW. Thermoacoustic engine. J. Acoust. Soc. Am. 1988;84:1145–80. https://doi.org/10.1121/1.396617.

[2] Petculescu A, Wilen LA. Oscillatory flow in jet pumps: Nonlinear effects and minor losses. J. Acoust. Soc. Am. 2003;113:1282–92. https://doi.org/10.1121/1.1543932.

[3] Zink F, Vipperman J, Schaefer L. CFD simulation of a thermoacoustic engine with coiled resonator. Int. Commun. Heat Mass Transf. 2010; 37:226–9. https://doi.org/10.1016/j.icheatmasstransfer.2009.09.001.

[4] Ueda Y, Yonemitsu S, Ohashi K, Okamoto T. Measurement and empirical evaluation of acoustic loss in tube with abrupt area change. J. Acoust. Soc. Am. 2020;147:364–70. https://doi.org/10.1121/10.0000597.

[5] Marx D, Mao X, Jaworski AJ. Acoustic coupling between the loudspeaker and the resonator in a standing-wave thermoacoustic device. Appl. Acoust. 2006;67:402–19. https://doi.org/10.1016/j.apacoust.2005.08.001.

[6] Olson JR, Swift GW. Energy dissipation in oscillating flow through straight and coiled pipes. J. Acoust. Soc. Am. 1996;100:2123–31. https://doi.org/10.1121/1.417922.

[7] Wee DST. PIV investigation of acoustic transmission through curved duct bends for the optimisation of thermoacoustic systems. PhD thesis, University of Nottingham, http://eprints.nottingham.ac.uk/29312/; 2015 [accessed 8 June 2022].

[8] Feng Y, Gao Y, Tang K, Jin T. Numerical investigation on turbulent oscillatory flow through a jet pump. J. Acoust. Soc. Am. 2019;145:1417–25. https://doi.org/10.1121/1.5094346.

[9] Yang P, Chen H, Liu Y. Numerical investigation on nonlinear effect and vortex formation of oscillatory flow throughout a short tube in a thermoacoustic Stirling engine. J. Appl. Phys. 2017;121: 214902. https://doi.org/10.1063/1.4984795.

[10] Thomas FO, Kozlov A, Corke TC. Plasma actuators for cylinder flow control and noise reduction. AIAA J. 2008;46:1921–31. https://doi.org/10.2514/1.27821.

[11] Roth JR, Sherman DM, Wilkinson SP. Electrohydrodynamic flow control with a glow discharge surface plasma. AIAA J. 2000;38:1166–72. https://doi.org/10.2514/2.1110.

[12] Moreau E. Airflow control by non-thermal plasma actuators. J. Phys. D 2007;40:605–36. https://doi.org/10.1088/0022-3727/40/3/S01.

[13] Cattafesta LN, Sheplak M. Actuators for active flow control. Annu. Rev. Fluid Mech. 2011;43:247–72. https://doi.org/10.1146/annurev-fluid-122109-160634.

[14] Yokoyama H, Otsuka K, Otake K, Nishikawara M, Yanada H. Control of cavity flow with acoustic radiation by an intermittently driven plasma actuator. Phys. Fluids 2020;32:106104. https://doi.org/10.1063/5.0017658.

[15] Yokoyama H, Omori Y, Kume M, Nishikawara M, Yanada H. Simulation of thermoacoustic heat pump effects driven by acoustic radiation in a cavity flow. Int. J. Heat Mass Transf. 2022;185: 122424. https://doi.org/10.1016/j.ijheatmasstransfer.2021.122424.

[16] Kishino Y, Yokoyama H, Omori H, Nishikawara M. Effects of stack position on thermoacoustic heat pump in a rectangular resonator. Proc. 26th International Congress on Sound and Vibration. Canada, 2019;348.

[17] Yokoyama H, Kobayashi M, Iida A. Analysis of flow and acoustic radiation in reed instruments by compressible flow simulation. Acoust. Sci. Tech. 2020; 41:739–50. https://doi.org/10.1250/ast.41.739.

[18] Wakeland RS, Keolian RM. Influence of velocity profile nonuniformity on minor losses for flow exiting thermoacoustic heat exchangers (L). J. Acoust. Soc. Am. 2002;112:1249–52. https://doi.org/10.1121/1.1502896.

[19] Merkli P, Thomann H. Transition to turbulence in oscillating pipe flow. J. Fluid Mech. 1975;68: 567–76. https://doi.org/10.1017/S0022112075001826.

[20] Inasawa A, Ninomiya C, Asai M. Suppression of tonal trailing-edge noise from an airfoil using a plasma actuator. AIAA J. 2013;51:1695–702. https://doi.org/10.2514/1.J052203.

[21] Murphy JP, Kriegseis J, Lavoie P. Scaling of maximum velocity, body force, and power consumption of dielectric barrier discharge plasma actuators via particle image velocimetry. J. Appl. Phys. 2013;113:243301. https://doi.org/10.1063/1.4811225.

[22] Thomas FO, Corke TC, Iqbal M, Kozlov A, Schatzman D. Optimization of dielectric barrier discharge plasma actuators for active aerodynamic flow control. AIAA J. 2009;47:2169–2178. https://doi.org/10.2514/1.41588.

[23] Steger, JL, Implicit finite-difference simulation of flow about arbitrary two-dimensional geometries, AIAA J. 1978;16:679–686. https://doi.org/10.2514/3.7377.

[24] Suzen YB, Huang PG, Jacob JD, Ashpis DE. Numerical simulations of plasma-based flow control applications. AIAA Paper 2005:2005-4633. https://doi.org/10.2514/6.2005-4633.

[25] Lele SK. Compact finite difference schemes with spectral-like resolution. J. Comput. Phys. 1992;103:16–42. https://doi.org/10.1016/0021-9991(92)90324-R.

[26] Swift GW, Thermoacoustics: A unifying perspective for some engines and refrigerators, second ed., Springer, Switzerland, 2002;77–147. https://doi.org/10.1007/978-3-319-66933-5.

[27] Forte M, Jolibois J, Pons J, Moreau E, Touchard G, Cazalens M. Optimization of a dielectric barrier discharge actuator by stationary and non-stationary measurements of the induced flow velocity: application to airflow control. Exp. Fluids 2007;43:917–28. https://doi.org/10.1007/s00348-007-0362-7.

[28] Rott N. Thermoacoustic. Adv. Appl. Mech. 1980;20:135–75. https://doi.org/10.1016/S0065-2156(08)70233-3.

[29] Fusco AM, Ward WC, Swift GW. Two-sensor power measurements in lossy ducts. J. Acoust. Soc. Am. 1992;91:2229–35. https://doi.org/10.1121/1.403656.

[30] Biwa T, Tashiro Y, Nomura H, Ueda Y, Yazaki T. Experimental verification of a two-sensor acoustic intensity measurement in lossy ducts. J. Acoust. Soc. Am. 2008;124:1584–90. https://doi.org/10.1121/1.2953311.

[31] Enloe CL, McLaughlin TE, VanDyken RD, Kachner KD. Mechanisms and responses of a single dielectric barrier plasma actuator: plasma morphology. AIAA J. 2004;42:589–94. https://doi.org/10.2514/1.2305.

[32] Miyamoto T, Yokoyama H, Iida A. Suppression of aerodynamic tonal noise from an automobile bonnet using a plasma actuator. SAE Int. J. Passeng. Cars - Mech. Syst. 2017;10:712–720. doi:10.4271/2017-01-1825

[33] Currie IG. Fundamental Mechanics of Fluids. McGraw-Hill, New York 1993:33–35.

[34] Yokoyama H, Tanimoto I, Iida A. Experimental tests and aeroacoustic simulations of the control of cavity tone by plasma actuators. Appl. Sci. 2017;7:790. https://doi.org/10.3390/app7080790.

[35] Kaneda I, Sekimoto S, Nonomura T, Asada K, Oyama A, Fujii K. An effective three-dimensional layout of actuation body force for separation control. Int. J. Aero. Eng. 2012;786960. https://doi.org/10.1155/2012/786960.